Numerical Insights Into the Influences of Chloride Baths Conditions on FeCoNi Ternary Alloy Electrodeposition

Shuai Zhang, Jing Yu[*], Zhaoyi Wang, Zhengda Liu*

Marine Engineering College, Dalian Maritime University, Dalian 116026, China;
[*]E-mail: yj.0730.kb@163.com

Electrodeposition of Fe-rich FeCoNi ternary alloys is an important and cost-effective surface fabrication method. It is necessary to investigate the influences of electrodeposition conditions in a systematic method. Finite element analysis (FEA) is an economical and time-saving way to study the numerous parameters during electrodeposition. In this work, the tertiary current distribution was used to model the codeposition of a FeCoNi ternary alloy, considering the intermediate absorption and hydrogen evolution reaction on the cathode. A comparative study between simulation and experiment in terms of the influences of operating conditions was conducted. Meanwhile, the experimental results validated the simulation models, showing excellent correspondence between the simulation and the experiment. Finally, the effects of operating conditions such as current density, bath temperature, bulk pH and electrolyte composition on cathode polarization, current efficiency, and throwing and covering power were investigated via simulation. The results can provide data for the industrial design and manufacture of FeCoNi alloy electrodeposition.

1. INTRODUCTION

Owing to their wide range of properties, iron group ternary alloys have attracted extensive attention in industry and academia[1-3]. The electrodeposition coating properties are largely dependent on the elemental composition. For instance, Fe-rich FeCoNi alloys have great potential in protective coatings for corrosion[4] and wear resistance[5], while Co-rich and Ni-rich alloys lead to high saturation magnetization and low coercivity[6]. FeCoNi alloys can be prepared by various methods, such as mechanical alloying[7], hydrogen plasma-metal reactions[8] and electrodeposition[9]. Electrodeposition is an economical and efficient technique to fabricate alloys and coatings because of the simple equipment and easy control of alloy compositions through modulating the electrolyte formulas and operating conditions[10].

Various electrolytes are applied in the deposition of iron group ternary alloys, such as metal chlorides, sulfate-based baths, sulfamate-chloride baths, and other baths with special additives. Co-rich and Ni-rich ternary alloys obtained from sulfate-based aqueous electrolytes have been extensively studied[11]. Due to their high current efficiency, simple electrolyte composition and low cost, chloride baths with no additives are industrially employed in Fe-based alloy deposition. To lower the internal stress of deposits from chloride baths, gradient structured coatings are fabricated using combined methods of alternating current (AC) activation and direct current (DC) deposition, as reported in our previous studies[12, 13]. Due to the very low pH values in chloride baths, the hydrogen evolution reaction is very intense at the cathode surface, thus reducing the cathodic current efficiency. In addition, the throwing power (TP)[14] and covering power (CP)[15, 16] of the electrolyte are important criteria for the deposition thickness uniformity, specifically on components with irregular geometries, such as crankshafts. However, there is a lack of relevant studies of FeCoNi alloy baths.

The codeposition of iron group metals (iron, cobalt and nickel) presents an anomalous phenomenon, which is characterized by the atomic fractions of the least or/and less noble metal exceeding its/their bulk (or mass) concentration in baths. To date, the mechanism of iron-group binary alloy (FeNi, FeCo, and NiCo) anomalous codeposition has been extensively investigated[17-19]. The anomalous codeposition of the FeCoNi ternary alloy is an irreversible two-step reaction mechanism. Because the various intermediates competitively adsorb on the cathode surface, the mechanism of anomalous codeposition of ternary alloys is complex. Although numerous experimental studies have been conducted on iron group ternary alloy deposition[5, 20-22], the majority relate to Co-rich and Ni-rich ternary alloys. In addition, limiting investigations focus on mathematical models and simulations of FeCoNi electrodeposition.

Numerous electrolyte compositions and operating conditions, such as metal ion concentration, current density, pH value, and bath temperature, impact the chemical composition, and thereby the coating properties. Therefore, controlling the electrodeposition of a ternary alloy is a complex matter. Multiphysical field coupling simulation is a cost- and time-saving method to develop and optimize the electrodeposition process. In addition, simulation can visualize the rarely observed experimental phenomena and thus help to unveil the electrode behaviour and deposition mechanism. Kamaraj et al.[23] modelled electrochemical additive manufacturing using the finite element method (FEM), revealing that migration and diffusion synthetically control the deposition process within the interelectrode gap. Giaccherini et al.[24] used COMSOL to investigate the current density distribution for aluminium deposition from molten salt. Electrolytes with additives are commonly used in metal deposition. However, few simulation models include the impact of additive adsorption at the cathode surface. Braun et al.[25] considered metal deposition as a function of additive (suppressor) coverage in their simulation model. In addition to numerically calculating the deposit thickness, simulation models can also be used to predict the elemental content[26] and to investigate the electrochemical behaviours via cyclic voltammetry (CV), chronoamperometry (CA), and square wave voltammetry (SWV)[27]. Until now, except for our previous preliminary study[13], there have been no studies on modelling the electrodeposition of iron group ternary alloys in a systematic manner. In addition, there are also no investigations on electrolyte bath properties (cathodic polarization behaviour, current efficiency, throwing power and covering power) via numerical modelling.

The adsorption of single-metal and mixed-metal intermediates at the cathode surface is an important reaction step of the electrodeposition of iron group ternary alloys. Simultaneously, the hydrogen evolution reaction occurs together with metal ion reduction. Therefore, in this study, we include the above two reactions in the simulation model. Elemental content is a substantial factor in determining the coating properties. Furthermore, the coating thickness is a crucial factor in determining satisfactory use in a given application. Therefore, we systematically investigated the influences of electrolyte composition and operational parameters on elemental content and coating thickness through a comparison of simulation and test results. In addition, the electrolyte polarization behaviour, current efficiency, throwing power and covering power were studied through finite element modelling.

2. EXPERIMENTAL PROCESS AND ELECTRODEPOSITION PARAMETERS

To comparatively study the influences of operating conditions on the coating thickness and elemental content, we designed a set of experiments, as shown in Table 1. The soluble anodes are four strips of commercial pure iron with dimensions of $230 \times 45 \times 10$ mm. The cathode is a rod of 42CrMo with dimensions of $\varPhi 25 \times 75$ mm. In industrial practice, several anodes are placed around the cathode to obtain a uniform electric field distribution. Thus, in the present study, we placed four anodes at each corner of the plating bath, as shown in Figure 1.
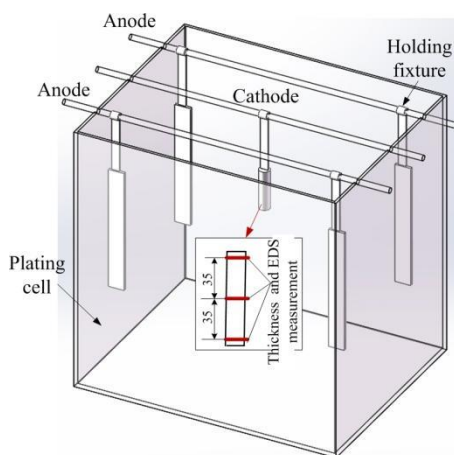

Figure 1. Schematic diagram of the electrodeposition setup and sample testing position

The electrodeposition was conducted in simple chloride metal salt baths without additives, including a fixed amount of 400 g/L $FeCl_2 \cdot 4H_2O$ together with varying amounts of $NiCl_2 \cdot 6H_2O$ and $CoCl_2 \cdot 7H_2O$. The electrolyte temperature was stabilized using a water bath, and the pH value was modulated using hydrochloric acid and sodium hydroxide.

A homemade power source, which can output alternating and direct current, was used for activation and deposition. The detailed electric parameters are shown in Figure 2. During the AC activation process, the grease and oxide layer can be removed, while a mildly dissoluble layer is formed

on the cathodic surface, which helps to form metallic bonding between the coating and substrate. As a result, the preparation procedures before electrodeposition are simplified. The following deposition process was conducted using DC mode, which in turn consists of low current, transitory phase and high current. The varying current density fabricates a gradient structured coating that is helpful to relieve the internal stress of thick deposited coatings. The electrodeposition duration of each experiment was 150 minutes, including 30 minutes of AC activation and 120 minutes of DC deposition. Notably, when studying the influence of the current density, we only modulate the high current stage, and the other stages remain the same.
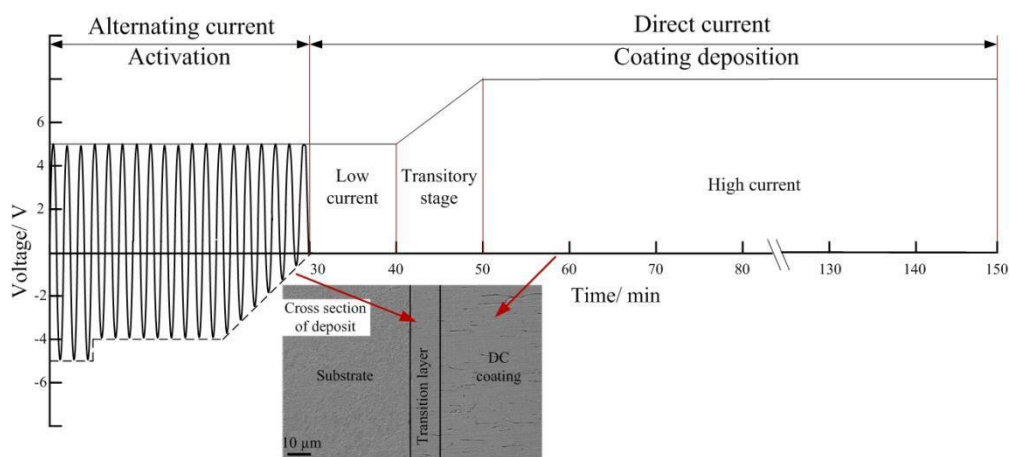

Figure 2. Diagram of the applied current density

Table 1. Electrodeposition operating parameters

Influence factor	Test no.	Electrolyte compound				Current density (A/dm^2)	Temperature °C	pH
		$NiCl_2 \cdot 6H_2O$		$CoCl_2 \cdot 7H_2O$				
		g/L	%	g/L	%			
Current density	C1	20	13.98	5	3.5	7.5	40	0.8
	C2					15		
	C3					18		
	C4					25		
Temperature	T1	20	13.98	5	3.5	15	35	0.8
	T2						40	
	T3						45	
	T4						50	
pH	P1	20	13.98	5	3.5	15	40	0.3
	P2							0.6
	P3							0.8
	P4							1
	P5							1.2
Ion concentration	I1	10	8.71	1.5	1.3	15	45	1
	I2	21	16.43	3.5	2.73			
	I3	32	22.97	4	2.86			
	I4	40	26.79	6	4			

The coating thickness was measured using an optical microscope (OM, GX51, OLYMPUS, Japan) at the cross section. The elemental composition was detected using energy dispersive X-ray spectrometry (EDS, Carl Zeiss NTS GmbH, Oberkochen, Germany) on the coating surface. The testing locations were from the upper, central, and lower parts of each deposited sample, as shown in Figure 1. For the cylindrical-shaped cathode, the electric field distributes relatively uniformly on the cylindrical surface. Thus, the average value is used for the experimental results.

3. NUMERICAL SIMULATION MODELS

3.1 Mathematical model

The electrodeposition process of the FeCoNi ternary alloy was modelled using the commercial multiphysics simulation software COMSOL$^@$6.0. The influences of the electrodeposition operating conditions on the coating properties (thickness and element composition) and electrolytic bath performance (polarization behaviour, current efficiency, throwing and covering power) were numerically investigated. The following assumptions were made:

(1)   All metal salts are completely dissolved in the electrolytic solution, which means that metal chlorides are electrolyzed into ionic species.

(2)   Due to the absence of extra stirring in the plating baths and the neglect of hydrogen gas desorption, convection is not considered in the electrolyte[28].

(3)   The adsorption of single metal and mixed metal intermediate species and hydrogen atoms are considered in the model, but their competitive adsorption is neglected[21].

(4)   Chloride ions are assumed not to adsorb on the cathode and thus do not participate in the electrodeposition reaction.

(5)   The calculation domain is the walls of the electrodeposition cell, which are assumed to be insulated.

In the studied electrolyte solution, the bulk concentrations of solutes are relatively low, representing dilute solutions. In addition, the influences of mass transport on the electrodeposition process and electrode kinetics are considered in the modelling. Therefore, the solver of the tertiary current distribution is applied in the numerical calculation.

For the electrodes, the relationship between current and voltage follows Ohm's law and conservation of current.

$$j_s = -\sigma_s \nabla \phi_s \qquad (1)$$
$$\nabla \cdot j_s = Q_s \qquad (2)$$

where j_s is the current density on the electrode surface, σ_s is the electrode conductivity, ϕ_s is the electrode potential, and Q_s is the general current source term.

In the tertiary current distribution, the current density of the electrolyte does not obey Ohm's law, and the ion gradient is taken into consideration. The current density in the electrolyte is governed by

$$j_l = F \sum_i z_i N_i \tag{3}$$

$$\nabla \cdot j_l = Q_l \tag{4}$$

where j_l is the current density of the electrolyte, z_i is the charge of the species, the subscript i refers to the electroactive species in the model (Fe^{2+}, Co^{2+}, Ni^{2+}, H^+, Cl^-), F is the Faraday constant, N_i is the ion species flux in the electrolyte, and Q_l is the general current source term.

The flux of each ion species follows the Nernst–Planck equation:

$$N_i = -D_i \nabla c_i - z_i u_i F c_i \nabla \phi_l \tag{5}$$

where u_i is the ionic mobility derived from $u_i = \frac{D_i}{kT}$; k is the Boltzmann constant; D_i is the diffusion coefficient, where the diffusion coefficients of Fe^{2+}, Co^{2+} and Ni^{2+} are 1.59×10^{-9} m^2/s, 1.21×10^{-9} m^2/s and 1.27×10^{-9} m^2/s, respectively[29]; c_i is the ion concentration; and ϕ_l is the potential in the electrolyte.
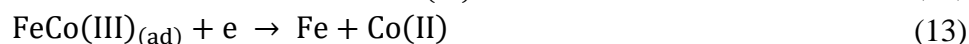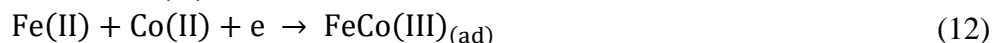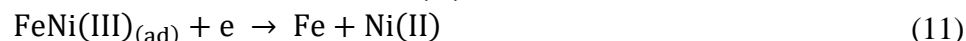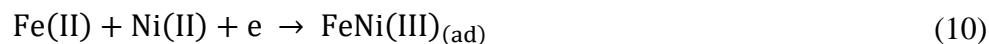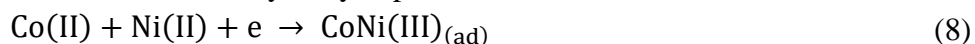
Within the metal ion diffusion layer, the material balance of each species at steady state is governed by:

$$\frac{dc_i}{dt} + \nabla \cdot N_i = 0 \tag{6}$$

The electroneutral state in the electrolyte is described as follows:

$$\sum_i z_i c_i = 0 \tag{7}$$

On the cathode surface, FeCoNi ternary alloy deposition follows electrochemical reactions[21]:

$$Co(II) + Ni(II) + e \rightarrow CoNi(III)_{(ad)} \tag{8}$$

$$CoNi(III)_{(ad)} + e \rightarrow Co + Ni(II) \tag{9}$$

$$Fe(II) + Ni(II) + e \rightarrow FeNi(III)_{(ad)} \tag{10}$$

$$FeNi(III)_{(ad)} + e \rightarrow Fe + Ni(II) \tag{11}$$

$$Fe(II) + Co(II) + e \rightarrow FeCo(III)_{(ad)} \tag{12}$$

$$FeCo(III)_{(ad)} + e \rightarrow Fe + Co(II) \tag{13}$$

Cathodic boundary conditions are solved using the Butler-Volmer equation, which involves concentration dependence.

$$j_{loc,m} = j_m \left(\frac{c_{m,red}}{c_m} exp\left(\frac{\alpha_a F \eta_m}{RT}\right) - \frac{c_{m,ox}}{c_m} exp\left(\frac{-\alpha_c F \eta_m}{RT}\right) \right) \tag{14}$$

where m represents Fe, Co, Ni, $j_{loc,m}$ is the local current density of the metal species, j_m is the exchange current density of the metal species, $c_{m,red}$ and $c_{m,ox}$ are the species concentrations in the deposits and on the electrode surface, respectively, c_m is the species concentration in the electrolyte, α_a and α_c are the transfer coefficients of the anode and cathode, respectively, and T is the bath temperature.

The overpotential η_m at the electrode/electrolyte interface is expressed by

$$\eta_m = \phi_s - \phi_l - E_{eq,m} \tag{15}$$

where $E_{eq,m}$ is the equilibrium potential between the electrode and electrolyte, determined by the Nernst equation

$$E_{eq,m} = E_m^\theta - \frac{RT}{nF} l\left(\frac{c_m}{c_{ref}}\right) \tag{16}$$

where E_m^θ refers to the standard electrode potential of the ion reduction reaction, $E_{Fe^{2+}}^\theta$ is −0.44 V, $E_{Co^{2+}}^\theta$ is −0.277 V, $E_{Ni^{2+}}^\theta$ is −0.25 V, $E_{H^+}^\theta$ is 0 V, and c_{ref} is the reference concentration (1 mol/L).

In addition to reactions 8 to 13, a hydrogen evolution reaction also occurred on the cathode, which is the dominant side reaction.

$$H^+ + e \rightarrow H_{(ad)} \tag{17}$$

$$H_{(ad)} + H^+ + e \rightarrow H_2 \tag{18}$$

The local current density in the hydrogen evolution reaction can be solved from the Tafel equation:

$$j_{loc,H} = -j_0 \times 10^{\eta_H/A_c} \tag{19}$$

where j_0 is the exchange current density of hydrogen gas ($2 \times 10^{-5} A/m^2$)[30] and A_c is the Tafel slope (-118 mV)[30]. η_H is the overpotential in the hydrogen evolution reaction. According to Equations (15) and (16), E_H^θ is zero.

Hydrogen production may hinder metal deposition by occupying the adsorption sites of intermediates[17]. Thus, the adsorption and surface blocking of hydrogen gas on the cathode surface is considered in the present model. Here, the hydrogen gas adsorbed on the cathode surface is considered as the suppressor, which can reduce the exchange current in metal ion reduction reactions, similar to additive consumption at the electrode/electrolyte interface treated by Braunn[25]. Therefore, the exchange current density is assumed to be a function of hydrogen coverage and metal ion concentration. Moreover, according to the definition of ternary iron-group metal anomalous codeposition, the reaction rate of the most noble species is inhibited, while that of the least noble species is enhanced. Depending on the bulk concentrations and deposition conditions, the deposition rate of Co exhibits either inhibition or enhancement[21]. Under the present experimental conditions, Co only presents an enhancement feature. The surface coverage of intermediates governs the deposition rate of metal species. Therefore, the exchange current density is assumed to be a function of hydrogen coverage and fraction surface coverage with respect to intermediate and metal ion bulk concentrations[25].

The exchange current density of metal species is described by

$$j_{Fe^{2+}} = [j_{Fe^{2+},unsupper}(1 - \theta_{H_2} - \theta_{CoNi(III)}) + j_{Fe^{2+},supper}(\theta_{H_2} + \theta_{CoNi(III)})]$$
$$\times \frac{c_{Fe^{2+}}^{0.75}}{c_{ref}} \tag{20}$$

$$j_{Co^{2+}} = [j_{Co^{2+},unsupper}(1 - \theta_{H_2} - \theta_{FeNi(III)}) + j_{Co^{2+},supper}(\theta_{H_2} + \theta_{FeNi(III)})]$$
$$\times \frac{c_{Co^{2+}}^{0.75}}{c_{ref}} \tag{21}$$

$$j_{Ni^{2+}} = [j_{Ni^{2+},unsupper}(1 - \theta_{H_2} - \theta_{FeCo(III)}) + j_{Ni^{2+},supper}(\theta_{H_2} + \theta_{FeCo(III)})]$$
$$\times \frac{c_{Ni^{2+}}^{0.75}}{c_{ref}} \tag{22}$$

where $j_{unsupper}$ is the exchange current density on the suppressed surface, where $j_{Fe^{2+},unsupper} = 120 A/m^2$, $j_{Co^{2+},unsupper} = 6.3 A/m^2$, $j_{Ni^{2+},unsupper} = 0.32 A/m^2$[21], and j_{supper} is the exchange current density on the suppressed surface, where $j_{Fe^{2+},supper} = 13 A/m^2$, $j_{Co^{2+},supper} = 0.87 A/m^2$, $j_{Ni^{2+},supper} = 0.03 A/m^2$. $\theta_{CoNi(III)}$, $\theta_{FeNi(III)}$ and $\theta_{FeCo(III)}$ represent the fraction surface

coverage by mixed metal intermediates, $\theta_{CoNi(III)} = 0.02$, $\theta_{FeNi(III)} = 0.42$, and $\theta_{FeCo(III)} = 0.21$[21], θ_{H_2} is the hydrogen coverage on the cathode surface, and $\theta_{H_2} = 1.1 \times 10^{-4}$ [31].

According to Faraday's law[32], the thickness of the coating is calculated by[33]

$$s_{tot} = \sum_m \frac{-j_{loc,m}}{zF} \frac{M_m}{\rho_m} t \tag{23}$$

where M_m is the molar mass, M_{Fe} is 56 g/mol, M_{Co} is 58.93 g/mol, M_{Ni} is 58.693 g/mol, ρ_i is the density, ρ_{Fe} is 7,900 kg/m³, ρ_{Co} is 8,900 kg/m³, and ρ_{Ni} is 8,910 kg/m³.

The atomic fraction of metal species (Fe, Co, Ni) in the deposited coating is calculated by

$$M(at.\%) = \frac{s_{tot,m}\rho_m/M_m}{\sum_m s_{tot,m}\rho_m/M_m} \tag{24}$$

The potential in the electrolyte along the anode is zero, while the potential in the electrolyte along the cathode surface is

$$-\frac{\partial \phi_l}{\partial n} = j_{loc,m} + j_{loc,H} \tag{25}$$

At the cathode surface, the local current density is solved from the boundary conditions of the flux of metal ion species and hydrogen ions:

$$N_m \cdot n = \frac{j_{loc,m}}{2F} \tag{26}$$

$$N_{H^+} \cdot n = \frac{j_{loc,H}}{F} \tag{27}$$

Along the insulating surface, the boundary condition is

$$N_i \cdot n = 0 \tag{28}$$

The initial conditions of reactant concentrations are

$$c_{Fe^{2+}} = c_{0,Fe^{2+}} \tag{29}$$

$$c_{Co^{2+}} = c_{0,Co^{2+}} \tag{30}$$

$$c_{Ni^{2+}} = c_{0,Ni^{2+}} \tag{31}$$

$$c_{H^+} = c_{0,H^+} \tag{32}$$

3.2 Mesh and independence check

To accurately simulate the anomalous codeposition behaviour on the cathode, the interfaces between the electrodes and electrolytic solution were refined using a highly fine triangular mesh, while the other calculation domain was meshed using a semirefined tetrahedral grid, as shown in Figure 3.

To balance the computational accuracy and resources, the independence of the grid and time step was tested. We calculated the deposition process under C2 conditions for 30 minutes with respect to different grids and time steps and then compared the coating thickness at three random points on the cathode, as shown in Figure 3. As the grid number increased from 68,411 to 83,421, the result differences were less than 0.13%, as shown in Figure 4(a). The time step size has no obvious impact on the calculation results, as plotted in Figure 4(b), indicating that the influence of the time step on the calculation results can be negligible. Thus, it is decided to use a grid number of 68,411 and a time step of 10 s in the following simulation.
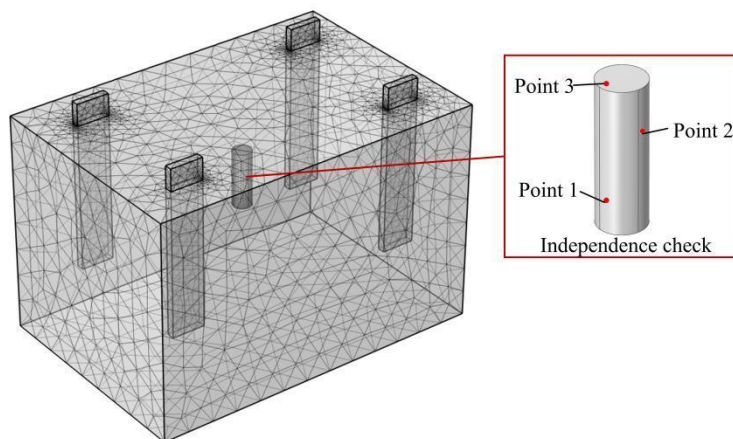
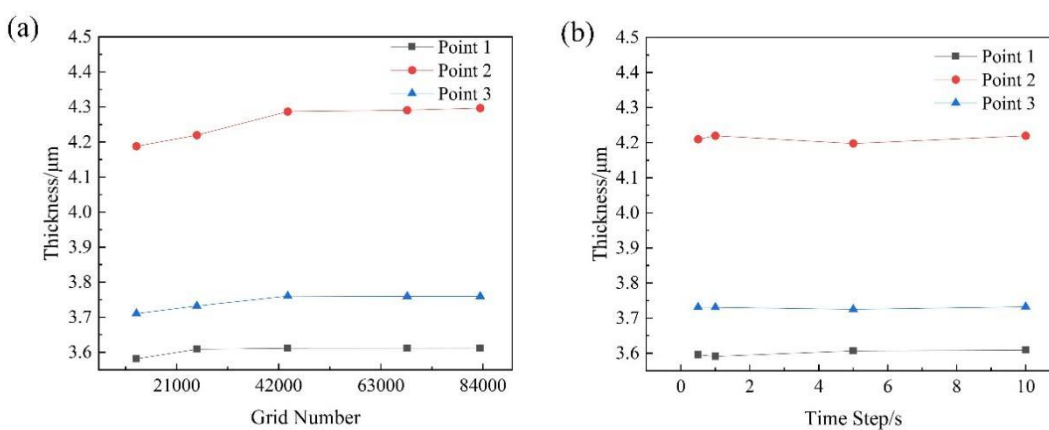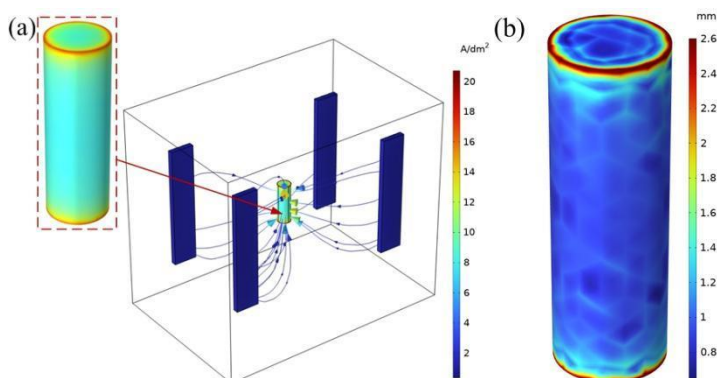**Figure 3.** Geometric model and computational mesh

Figure 4. Independence study of grid number (a) and time step (b) under C2 conditions for 30 min

4. RESULTS AND DISCUSSION

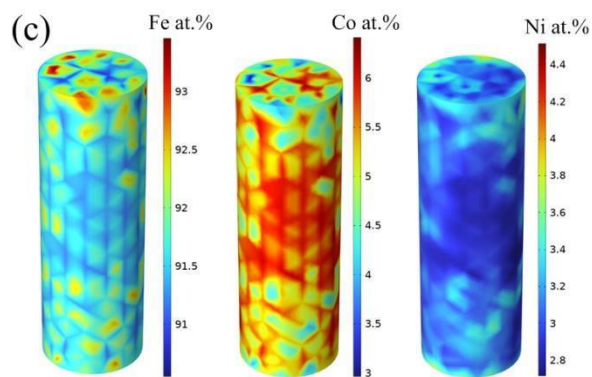*4.1 Simulated electrodeposition behaviour*

Figure 5 Simulated (a) electric field, (b) coating thickness, and (c) element content under C2 conditions at *t*=150 min

Figure 5 shows the distributions of the current density, coating thickness and element content as the electrodeposition experiment was conducted under C2 conditions at *t*=150 min. Even though the cathode is a round bar with a simple geometry, the current density distribution is slightly uneven at the cylindrical surface and the top and bottom surfaces. It can be observed that the current density concentrates at the edge (Figure 5(a)). According to Faraday's law, the coating thickness presents the same distribution as the electric field. The thickness on the cylindrical surface is relatively smoother than that on the top and bottom ends (Figure 5(b)). Interestingly, the element contents in deposition showed an inhomogeneous distribution (Figure 5(c)), especially the Co content. In addition, the chemical compositions displayed different distribution states with current density. The metal element distribution is much related to the side reactions on the cathode and the electrochemical properties of the electrolyte[34].
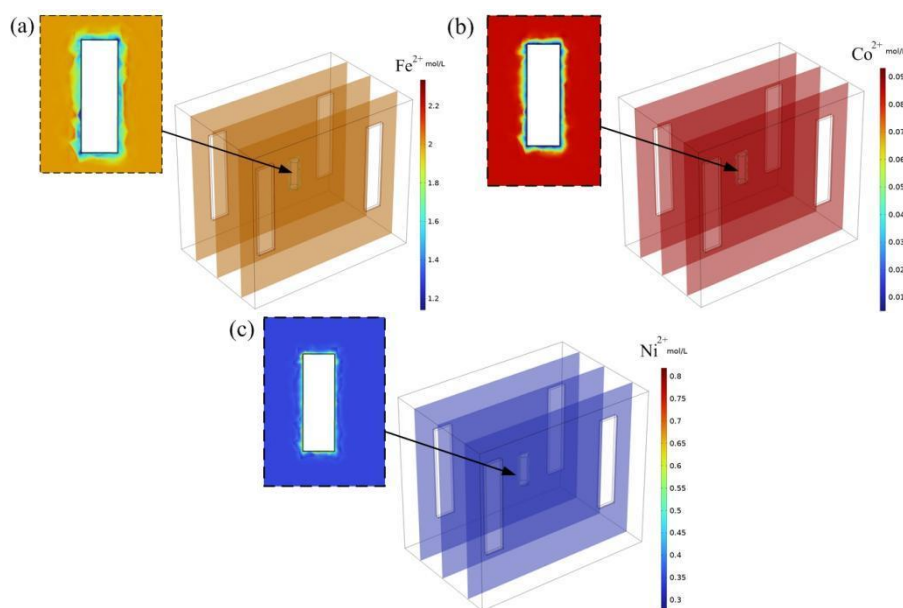

Figure 6. Metal ion concentration near the cathode surface: (a) Fe^{2+}, (b) Co^{2+}, and (c) Ni^{2+} under C2 conditions at *t*=100 min

The distributions of metal ion concentrations in the electrolyte are shown in Figure 6 through cross-sectional views. Drastic concentration gradients can be observed near the cathode surface during the electrodeposition process. The ion concentrations of Fe^{2+} and Co^{2+} near the cathode surface are significantly lower than those in the electrolyte. In contrast, the Ni^{2+} concentration shows an inverse distribution state. The above metal ion distributions indicate that Fe and Co deposition are governed by mass transport, while Ni deposition is an electric field-controlled process. Additionally, these ion concentration gradients also reveal the abnormal codeposition of iron group metals under the present operating conditions.

4.2 Comparative investigation of the influences of the electrodeposition operating conditions
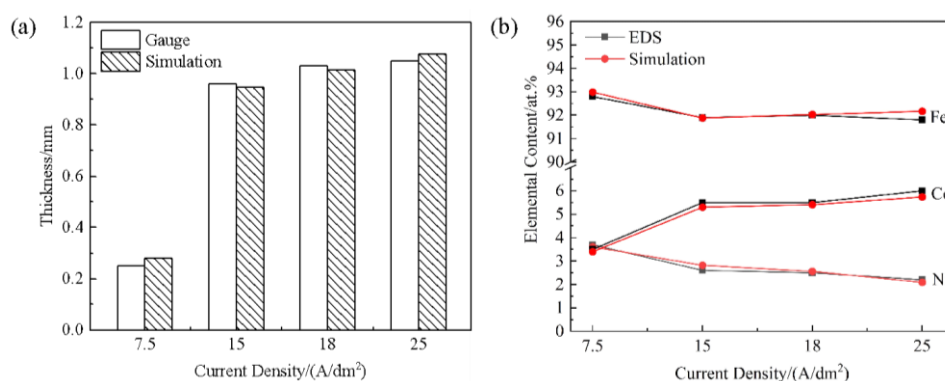

Figure 7. Simulated and experimental (a) thickness and (b) element content of the deposited coating at varying current densities, 40 °C, pH 0.8 for 150 min with the concentration of 20 g/L $NiCl_2 \cdot 6H_2O$ and 5 g/L $CoCl_2 \cdot 7H_2O$

The coating thickness varies with the applied current density, as shown in Figure 7(a). It can be observed that both the measured and simulated thicknesses increase nonlinearly with increasing current density. In addition, at relatively low (7.5 A/dm^2) and high (25 A/dm^2) current densities, the measured thicknesses are smaller than the simulated values. In contrast, the measured thicknesses are larger than the simulated thicknesses at current densities of 15 A/dm^2 and 20 A/dm^2. At low current density, the thickness of the double layer contributes largely to the whole deposited layer. However, until now, the simulation software has not perfectly addressed the double layer[33]. At a high current density, the hydrogen evolution reaction is more intense, and convection on the cathode surface occurs. However, hydrogen gas desorption was neglected in the simulation modelling.

The influence of the current density on the element content is displayed in Figure 7(b). The Fe content in the deposited coating decreases as the current density increases from 7.5 A/dm^2 to 15 A/dm^2 and then tends to remain stable as the current density increases. The Co content in the coating first increases quickly and then increases slowly as the current density increases. In contrast, the Ni content presents the reverse change trend. The simulated element content was extremely close to the measured EDS values.
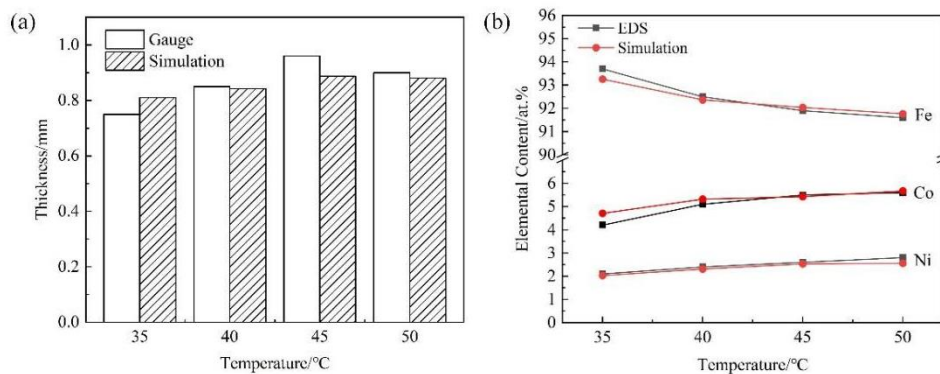
Figure 8. Simulated and experimental (a) thickness and (b) element content of the deposited coating at varying temperatures, 15 A/dm^2, pH 0.8 for 150 min with the concentration of 20 g/L NiCl$_2$·6H$_2$O and 5 g/L CoCl$_2$·7H$_2$O

The coating thickness increases as the bath temperature increases from 35 °C to 45 °C and then decreases as the temperature continuously increases, as shown in Figure 8(a). The Fe content in the deposit decreases obviously with increasing bath temperature. The influences of bath temperature on the coating thickness and element content are plotted in Figure 8(b). The measured Co content increases gradually as the bath temperature increases from 35 °C to 45 °C and then tends to remain unchanged with increasing bath temperature. With increasing bath temperature, the Ni content remains nearly unchanged. From the element content variation, it can be found that the degree of anomalous codeposition behaviour decreases at relatively high temperatures. During a real electrodeposition experiment, ferrous ions (Fe^{2+}) easily convert to ferric ions (Fe^{3+}) at a relatively high bath temperature, which in turn form the precipitate of the metal hydroxide of Fe, namely, Fe(OH)$_3$, adsorbing onto the cathode surface[20]. This phenomenon cannot be included in modelling.
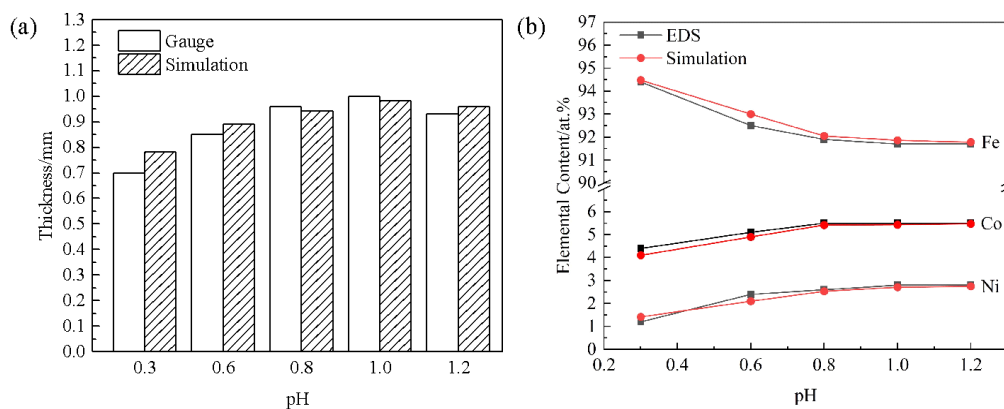

Figure 9. Simulated and experimental (a) thickness and (b) element content of the deposited coating at different bath pH values, 15 A/dm^2, 40 °C for 150 min with the concentration of 20 g/L NiCl$_2$·6H$_2$O and 5 g/L CoCl$_2$·7H$_2$O

The influences of bath pH values on the coating thickness and element content are displayed in Figure 9. The deposit thickness increases as the bath pH value increases from 0.3 to 1.0 and then decreases slightly at a pH value of 1.2. Under stronger acidic electrolytic conditions, the hydrogen evolution reaction on the cathode surface is extremely intense, which results in lower current efficiency. Therefore, a thinner coating thickness is obtained in this scenario.

As reported in ref.[35], the bath pH value has a strong influence on the element composition in electrodeposits. The Fe content decreases as the pH value increases. In contrast, the Co and Ni contents show an inverse change trend. At a relatively low bath pH, the element content is sensitive to the amount of hydrogen gas adsorption on the cathode surface. With the increase in pH value, the adsorption of hydrogen gas did not affect the deposit composition[37], while the adsorption of metal ions dominated. Therefore, the element content tended to be stable as the bath pH increased from 0.8 to 1.2. Li et al.[36] reported that the intermediates were metal hydroxides of Fe, Co and Ni even in a strongly acidic solution in the electrodeposition of Fe-Ni-Co nanowires. The dissociation of aqueous solvent was not included in the present modelling. As a result, there were no intermediates of metal hydroxides adsorbed on the cathode surface. This simplification may cause the difference between the simulation and experiment.
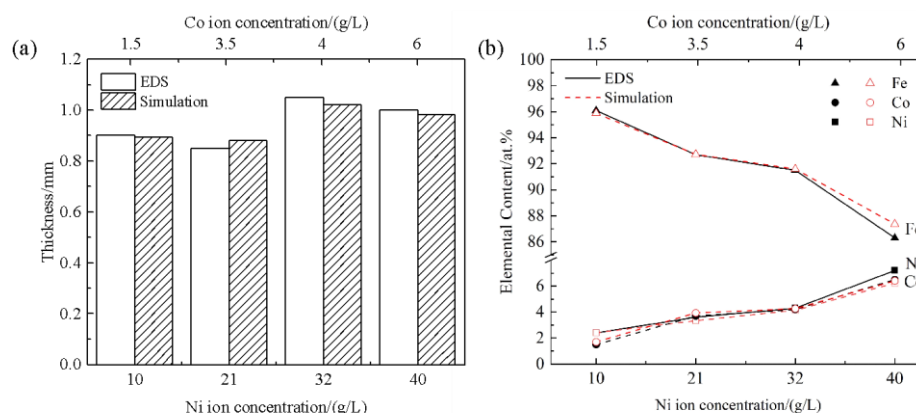

Figure 10. Simulated and experimental (a) thickness and (b) element content of the deposited coating with different electrolyte concentrations, at 15 A/dm^2, 45 °C, pH 1 for 150 min

The coating thickness increases with increasing Ni and Co concentrations in the electrolyte, as shown in Figure 10(a). Note that although the total metal ion concentration is higher in the I2 (21/3.5) electrolyte than in the I1 (10/1.5) electrolyte, the coating thickness is greater in the latter electrolytic bath. It is presumed that the ratio of Ni/Co dominates the coating thickness compared to the total ion concentration at relatively lower ion concentrations, similar to the results reported in ref.[37]. The element content in the deposits varies with the Ni and Co concentrations in the electrolyte as plotted in Figure 10(b). The Fe content in the deposits decreases as the Ni and Co concentrations increase. In contrast, Ni and Co contents in deposits show reverse trends. Due to the anomalous nature of iron group element codeposition, a very low Co content in the electrolyte results in a high Co content in the deposit[38].

The average values of coating thickness and element content are used to calculate the percentage error between simulation and experiment[38]. The maximum errors and possible causes that may lead

to the errors are summarized in Table 2. The comparison shows that the general agreement between the simulation and measured results is within 14%, which is an acceptable error in the engineering field[39]. In general, although some assumptions and simplifications were made, the simulated and experimental coating thicknesses and element contents display similar change trends. Therefore, we employ the same finite element model to assess the following bath properties.

Table 2. Error between simulation and experiment and possible causes

	Maximum percentage error/%				Possible causes
	Thickness	Elemental content			
		Fe	Co	Ni	
Current density (see Figure 7)	12	0.4	4.3	8.5	① The thickness of the double layer[33] ② Constant surface coverage coefficient of intermediates ③ Charge transfer coefficient on the cathodes derived from extrapolation in the nonlinear Tafel region[38]
Temperature (see Figure 8)	7.6	0.5	12.1	8.6	① A fixed diffusion coefficient taken from reference[9] ② Oxidation of Fe^{2+} into Fe^{3+} at higher bath temperature
Bath pH (see Figure 9)	11.4	1.6	6.8	12.5	The reduction of aqueous solvent is not included.
Ion concentration (see Figure 10)	3.6	1.2	13.6	13.5	Neglect of convection

4.3 Investigation of bath performance via simulation

4.3.1 Polarization behavior

The steady-state polarization curves of FeCoNi electrodeposited under various operating conditions and electrolyte concentrations generated via simulation are shown in Figure 11. Figure 11(a) shows the cathode polarization curves of the FeCoNi alloy and individual metal electrodeposition. When the current density is less than approximately 3.8 A/dm^2, the j-E curve of alloy deposition lies between those of Co and Fe, and the magnitude of polarization of individual metals is in accord with the noble order of the element. As the current density increases, the j-E curve of the ternary alloy deposition moves in a more positive direction, indicating that the codeposition allows iron and cobalt to deposit at more positive potentials while causing nickel to reduce at more negative potentials[14]. A slight change in cathode polarization is observed with increasing bath temperature, as plotted in Figure 11(b). The migration and diffusion of metal ions are accelerated with increasing bath temperature, resulting in weaker polarization on the cathode surface[40]. As the bath pH values increased from 0.3 to 1.2, the

cathode polarization curve shifted in a more negative direction, which means that the degree of cathode polarization increased, as shown in Figure 11(c). At lower bath pH values, the cathode polarization is governed by the hydrogen discharge[41]. With increasing electrolyte concentration, the cathode polarization tended to be significantly weaker, as shown in Figure 11(d).
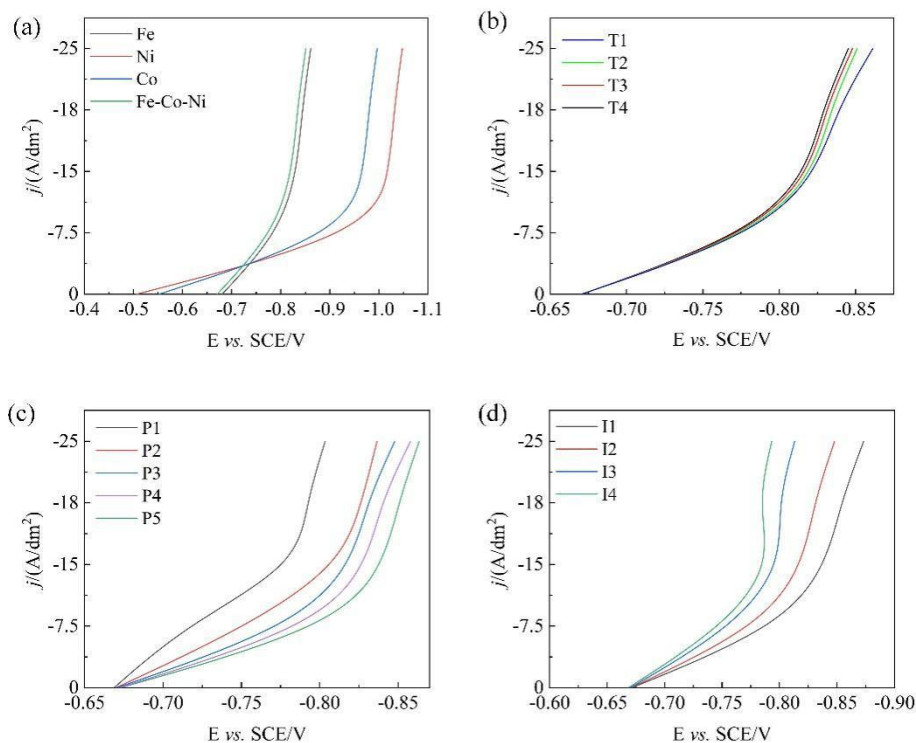

Figure 11. Steady-state polarization curves under different operating conditions: (a) current density, (b) bath temperature, (c) pH, (d) electrolyte concentration

4.3.2 Cathodic current efficiency

During the electrodeposition of FeCoNi alloys, alloy deposition accompanied by side reactions, such as hydrogen evolution and the reduction of aqueous solvent, occurs on the cathode surface. Therefore, the current efficiency of alloy deposition is always below 100%. Additionally, the cathodic current efficiency is an important economic indicator of energy efficiency. The current efficiency of alloy and single metal deposition is calculated by[42]

$$CCE\% = \frac{Q_{c,m}}{Q_a} \times 100\% = \frac{j_{loc,m}At}{\left(\sum_m j_{loc,m} + j_{loc,H}\right)At} \tag{33}$$

where $Q_{c,m}$ is the electric charge used for alloy or individual metal deposition, Q_a is the total electric charge during the electrodeposition process, A is the cathode area immersed in the electrolyte, and t is the deposition time.
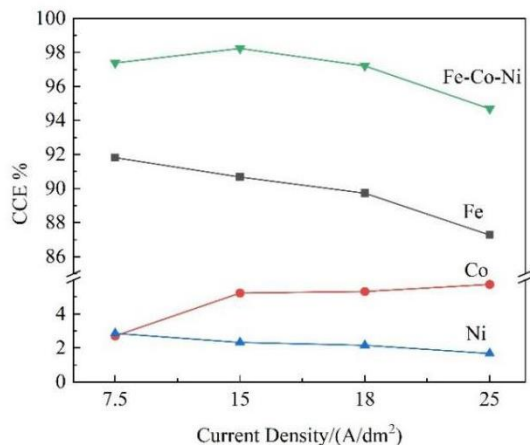
Figure 12. Effect of current density on current efficiency. Electrodeposition was conducted at 40 °C, pH 0.8 for 150 min with the concentration of 20 g/L $NiCl_2 \cdot 6H_2O$ and 5 g/L $CoCl_2 \cdot 7H_2O$.

Figure 12 shows the effect of the current density on the current efficiency of alloys and individual metal deposition. As the current density increased from 7.5 A/dm^2 to 15 A/dm^2, the current efficiency of the alloy increased slightly, reached a maximum value of 98%, and then decreased rapidly as the current density continuously increased. A higher current density leads to increasing cathode polarization close to the deposition potential of Co. Consequently, the partial efficiency of Co increases. As the current density further increased, the hydrogen evolution reaction became more intense and thus blocked the adsorption sites of metal intermediates[43]. As a consequence, the current efficiency of alloy deposition decreased.
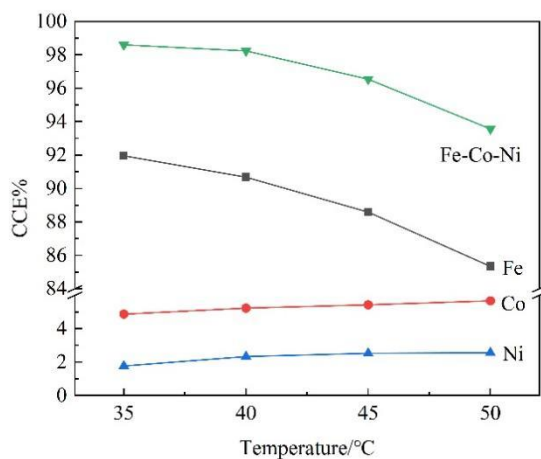

Figure 13. Effect of bath temperature on current efficiency. Electrodeposition was conducted at 15 A/dm^2, pH 0.8 for 150 min with the concentration of 20 g/L $NiCl_2 \cdot 6H_2O$ and 5 g/L $CoCl_2 \cdot 7H_2O$

Figure 13 shows the current efficiency of alloy deposition, together with the partial efficiency of a single metal. At the beginning of the temperature rise to 40 °C, the current efficiency of the alloy decreased slowly. Subsequently, the current efficiency showed a rapid decrease. It is known that a higher bath temperature leads to more serious hydrogen evolution[42], which may result in a decrease in the current efficiency. In addition, due to the reduction in polarization with increasing bath temperature[44], the partial efficiency of Fe deposition decreased, and that of Co and Ni increased. The element contents in deposits showed a similar tendency with respect to bath temperature (see Fig. 8).
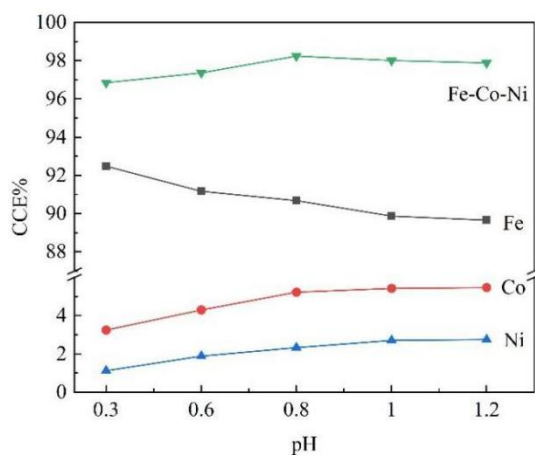

Figure 14. Current efficiency at varying bath pH values. Electrodeposition was conducted at 15 A/dm^2, 40 °C for 150 min with the concentration of 20 g/L NiCl$_2$·6H$_2$O and 5 g/L CoCl$_2$·7H$_2$O

Figure 14 shows the variation in current efficiency with bath pH value. The current efficiency of alloy deposition changed slightly with the pH value, while the partial efficiency of individual metals showed drastic changes. In this study, the bath pH values range from 0.3 to 1.2: namely, more highly acidic electrolyte baths are employed. At lower bath pH values, the reduced metallic atoms are easily dissolved, while the formation and adsorption of metal intermediates on the cathode surface are difficult. The electrodeposition of iron group alloys tends to be normal in strongly acidic plating baths[45], wherein the deposition of the least noble metal (iron) is hindered; in contrast, that of noble and less noble metals (nickel and cobalt) is promoted.
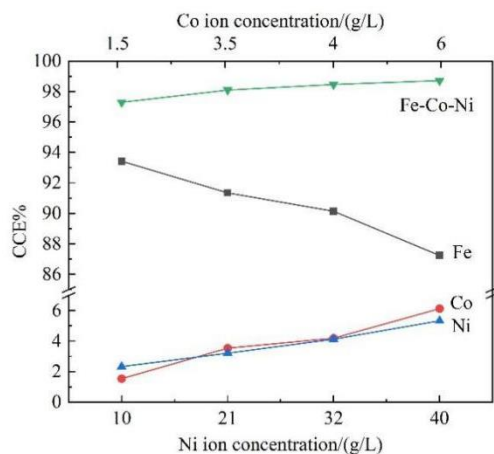
Figure 15. Influences of electrolyte concentration on the current efficiency of the alloy and single metal. Electrodeposition was conducted at 15 A/dm², 45 °C, pH 1 for 150 min.

Figure 15 shows that the current efficiency for alloy deposition slightly increased with electrolyte concentration, which was the result of the decrease in the partial efficiency of Fe and the increase in the partial efficiency of Co and Ni. As the electrolyte concentration increased, the cathode polarization significantly decreased[40], closely approaching the reduction potential of Ni and Co. Consequently, the partial efficiency of Fe deposition sharply decreased, while those of Co and Ni drastically increased.

4.3.3 Throwing power and covering power

Throwing power (TP) is an important criterion to evaluate the uniformity of coating thickness. The influences of the electrolyte and operating conditions on the throwing power of FeCoNi electrodeposition were quantitatively investigated by simulation. In industrial practice, a Haring-Blum cell is used with the help of Field's empirical formula[46, 47] to measure the TP values of a plating bath[41]. The simulation model is shown in Figure 16.

$$TP\% = \frac{(K - B)}{(K + B - 2)} \times 100\% \qquad (34)$$

where K is the current distribution ratio, $K = \frac{x_1}{x_2}$, B is the metal distribution ratio, $B = \frac{w_2}{w_1}$, $x_1 \ and \ x_2$ are the distances between the anode and cathode, and w_1 and w_2 are the weights of the deposits on the far and near cathodes obtained from the simulation, respectively. Usually, the distance ratio is set between 1:1 and 5:1[41]; here, we used $x_1 : x_2 = 2 : 1$.
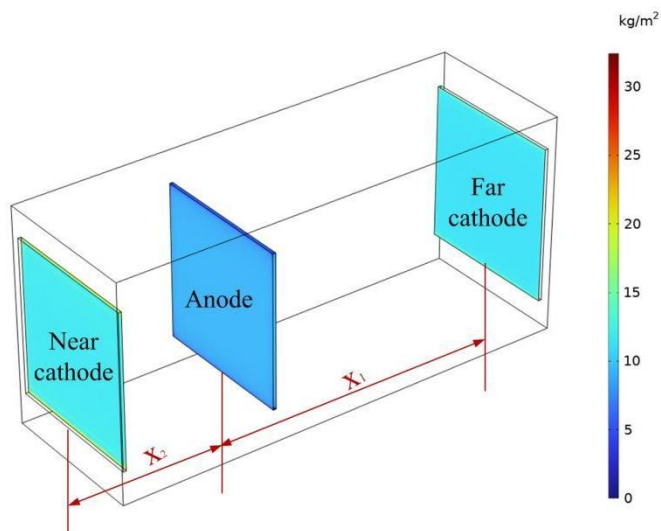
Figure 16. Schematic of the Haring-Blum cell test

Covering power (CP) is also a crucial criterion to evaluate the electrodeposition capacity, specifically for deposition on a complex geometry. According to industrial standards[48], a right-angled cathode is placed on one side of the plating bath, as shown in Figure 17. The ratio of the deposited area to the cathode surface area is used to evaluate the covering power[16]:

$$CP\% = \frac{S}{S_{tot}} \times 100\% \tag{35}$$

where S is the area covered with alloys and S_{tot} is the area of the cathode surface.
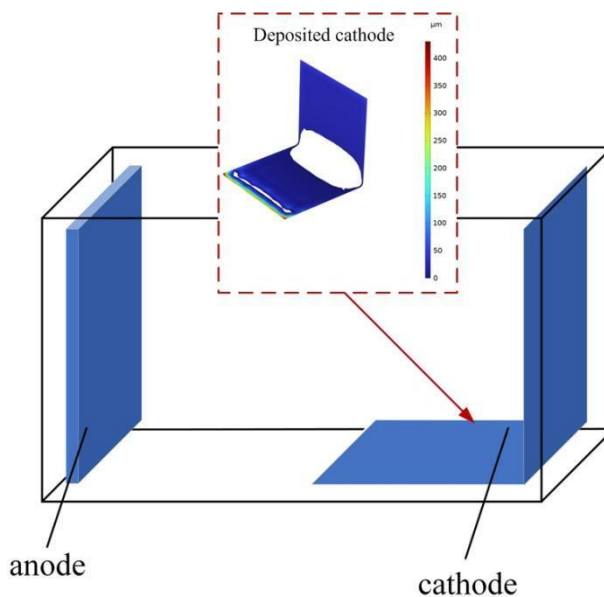

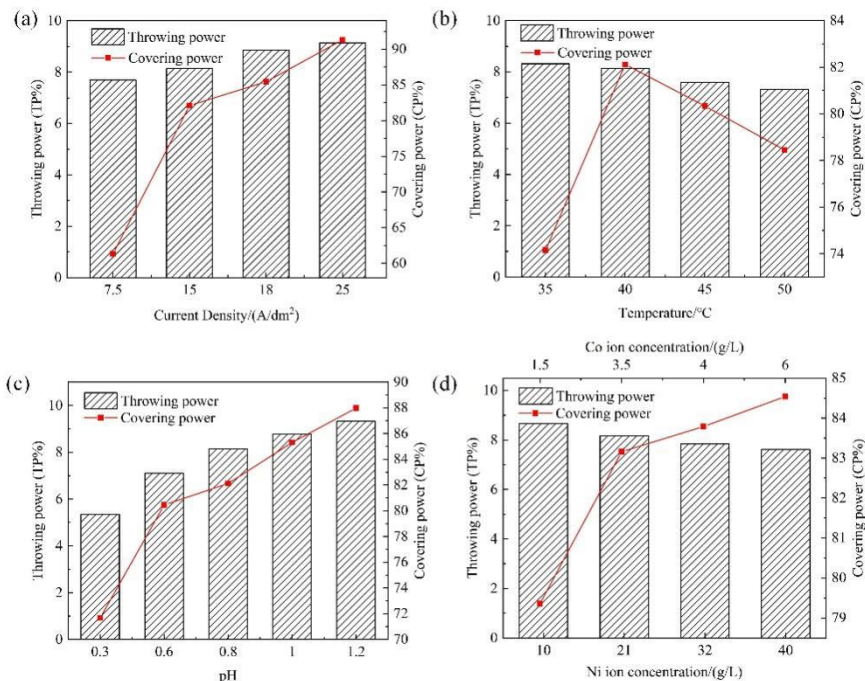**Figure 17.** Schematic of the covering power test

Figure 18. Throwing power and covering power under various operating conditions: (a) current density, (b) bath temperature, (c) electrolyte pH and (d) bulk concentrations

The impacts of the current density, bath temperature, pH and bulk concentration on the throwing power and covering power are shown in Figure 18. The throwing power is mainly determined by the cathode polarization and the electrolyte conductivity. The covering power is primarily determined by the deposition potential and the electrochemical properties of the electrolyte[16]. It can be observed that the TP values of the studied FeCoNi plating baths are relatively low. Limiting investigations on the throwing power of iron group alloy electrodeposition using a similar evaluation method as employed in this study reported that the NiCo alloy plating baths[14] showed very poor throwing power (the TP values are below zero). When the current density increased from 7.5 A/dm^2 to 25 A/dm^2, the TP value increased from 7.69% to 9.14%, while the CP value increased from 61.35% to 91.32% (Figure 18(a)). As the bath temperature increased, the TP value decreased gradually from 8.32% to 7.31%. The CP value reached 82.12% at 40 °C and then decreased to 78.45% at 50 °C (Figure 18(b)). As the pH values increased from 0.3 to 1.2, the TP value and CP value increased drastically from 5.34% to 9.32% and from 71.68% to 87.98%, respectively (Figure 18(c)). As the electrolyte concentration increased, the TP value decreased slightly from 8.67% to 7.62%. In contrast, the CP value increased from 79.36% to 84.54% (Figure 18(d)). For the operating conditions of current density and pH, the throwing power and covering power were positively correlated. Additionally, better throwing power corresponded to better covering power. In contrast, the throwing power was inversely proportional to the bath temperature and bulk concentration. Moreover, there were no clear corresponding relations between the throwing power and covering power.

5. CONCLUSIONS

In this work, the electrodeposition processes of a FeCoNi ternary alloy were modelled using the finite element method. The tertiary current distribution was employed in the modelling, considering intermediate adsorption and hydrogen evolution on the cathode. Some conclusions are drawn from the study and summarized as follows:

(1) From the simulated electrodeposition behaviour, it can be observed that the even electric field distribution resulted in an even coating thickness, except for the edges of the top and bottom ends. However, the element content in deposits presented a different distribution with current density. In addition, the ion concentration gradients reveal that the FeCoNi codeposition showed abnormal behaviour under the studied operating conditions.

(2) Comparative studies of the influences of electrodeposition operating conditions between the simulation and experiments were conducted. Meanwhile, the simulation model was validated by comparing the coating thickness and element content in the deposits. The calculated results showed good consistency with the experimental results.

(3) The influences of current density, bath temperature, bulk pH and electrolyte concentration on the performance of electrolytic baths were investigated via simulation in a systematic manner. The resultant data are helpful in the process design and manufacture of industrial electrodeposition.

References

1. K.M. Hyie, M.Z. Zabri, N.R.N. Roseley and N.R.N.M. Masdek, *J. Mater. Res.*, 31 (2016) 1848.
2. S.P. Harimkar, S.R. Bakshi and A. Agarwal, *JOM*, 65 (2013) 739.
3. V. Torabinejad, M. Aliofkhazraei, A.S. Rouhaghdam and M.H. Allahyarzadeh, *Tribol. Int.*, 106 (2017) 34.
4. B.Y. Yoo, S.C. Hernandez, D.Y. Park and N.V. Myung, *Electrochim. Acta*, 51 (2006) 6346.
5. M.S. Md.Nor, Z. Salleh, N.R.N.M. Masdek, Y.M. Taib, K.M. Hyie and M.Z. Abu, *Mater. Today:. Proc.*, 46 (2021) 1792.
6. P. Ledwig, M. Kac, A. Kopia, J. Falkus and B. Dubiel, *Materials*, 14 (2021) 3886.
7. E. Jartych, *J. Magn. Magn. Mater.*, 323 (2011) 209.
8. X. Li and S. Takahashi, *J. Magn. Magn. Mater.*, 214 (2000) 195.
9. A.I.N. Turmiasaputri, H. Erfan and S. Budi, *Chem. Mater.*, 1 (2022) 61.
10. Y. Li, X. Cai, G. Zhang, C. Xu, W. Guo and M. An, *J. Alloys Compd.*, 903 (2022) 163761.
11. S. Budi, S. Muhab, A. Purwanto, B. Kurniawan and A. Manaf, *Mater. Sci.-Pol.*, 37 (2019) 389.
12. R. Huang, Z. Ma, W. Dong, Y. Shen, F. Du, J. Xu and M. Jin, *Strength Mater.*, 51 (2019) 280.
13. S. Zhang, J. Yu, Z. Liu, Y. Yin and C. Qiao, *Materials*, 15 (2022) 6141.
14. R.M. Al Radadi and M.A.M. Ibrahim, *Korean J. Chem. Eng.*, 37 (2020) 1599.

Int. J. Electrochem. Sci., 17 **(2022)** Article Number: 221252

22

15. B.S. Pan and Y. Yang, *Key Eng. Mater.*, 359-360 (2008) 68.
16. H. Wang, J. Tang, G. Li, C. Zhang, J. Zhu, Z. Wang, G. Ding and X. Zhao, *J. Micromech. Microeng.*, 20 (2010) 115024.
17. K.Y. Sasaki and J.B. Talbot, *J. Electrochem. Soc.*, 147 (2000) 189.
18. N. Zech, E. Podlaha and D. Landolt, *J. Electrochem. Soc.*, 146 (1999) 2892.
19. H. Dahms and I. Croll, *J. Electrochem. Soc.*, 112 (1965) 771.
20. Y. Yang, *Int. J. Electrochem. Sci*, 2015. 10 (2015) 5164.
21. Y. Zhuang and E. Podlaha, *J. Electrochem. Soc.*, 150 (2003) C225.
22. N. Zech, E. Podlaha and D. Landolt, *J. Electrochem. Soc.*, 146 (1999) 2886.
23. A. Kamaraj, S. Lewis and M. Sundaram, *Procedia CIRP*, 42 (2016) 788.
24. A. Giaccherini, S. Caporali, E. Berretti, P. Marcantelli, I. Sanzari, I. Perissi and M. Innocenti, *ECS Trans.*, 64 (2015) 1.
25. T.M. Braun, D. Josell, J. John and T.P. Moffat, *J. Electrochem. Soc.*, 167 (2019) 013510.
26. C.V. Manzano, P. Schürch, L. Pethö, G. Bürki, J. Michler and L. Philippe, *J. Electrochem. Soc.*, 166 (2019) E310.
27. M. Zhang, J. Wang, Y. Cai, C. Jiao, S.O. Adede and C. Zhu, *J. Electrochem. Soc.*, 166 (2019) D868.
28. S. Palli and S.R. Dey, *Int. J. Electrochem.*, 2016 (2016) 3482406.
29. D. Yuan, Y. Liu, G. Liu and Y, Tong, *Journal of Jinan University*(*Natural Science*), 25 (2004) 346. (in Chinese)
30. B. Yue, G. Zhu, Y. Wang, J. Song, Z. Chang, N. Guo and M. Xu, *J. Electroanal. Chem.*, 891 (2021) 115274.
31. C. Gabrielli, P.P. Grand, A. Lasia and H. Perrot, *J. Electrochem. Soc.*, 151 (2004) A1925.
32. G. Yang, D. Deng, Y. Zhang, Q. Zhu and J. Cai, *Electrocatalysis*, 12 (2021) 478.
33. A. Mahapatro and S. Kumar Suggu, *Adv. Mater. Sci.*, 3 (2018) 1.
34. S. Eugénio, T.M. Silva, M.J. Carmezim, R.G. Duarte and M.F. Montemor, *J. Appl. Electrochem.*, 44 (2013) 455.
35. R. Oriňáková, A. Oriňák, G. Vering, I. Talian, R.M. Smith and H.F. Arlinghaus, *Thin Solid Films*, 516 (2008) 3045.
36. D. Li and E. Podlaha, *J. Electrochem. Soc.*, 164 (2017) D843.
37. J. Pang, Q. Li, W. Wang, X. Xu and J. Zhai, *Surf. Coat. Technol.*, 205 (2011) 4237.
38. I. Belov, C. Zanella and C. Edström, P. Leisner, *Mater. Des.*, 90 (2016) 693.
39. N. Hongkarnjanakul, C. Bouvet and S. Rivallant, *Compos. Struct.*, 106 (2013) 549.
40. é.M. Natanson, T.M. Shvets, Z.M. Mel"Nichenko and V.S. Sperkach, *Powder Metall. Met. Ceram.*, 10 (1971) 347.
41. M.A.M. Ibrahim and R.M. Al Radadi, *Mater. Chem. Phys.*, 151 (2015) 222.
42. X. Qiao, H. Li, W. Zhao and D. Li, *Electrochim. Acta*, 89 (2013) 771.
43. P. Fricoteaux and C. Rousse, *J. Electroanal. Chem.*, 612 (2008) 9.
44. M.H. Seo, D.J. Kim and J.S. Kim, *Thin Solid Films*, 489 (2005) 122.
45. I. Khazi and U. Mescheder, *Mater. Res. Express*, 6 (2019) 082001.
46. V. Torabinejad, M. Aliofkhazraei, S. Assareh, M.H. Allahyarzadeh and A.S. Rouhaghdam, *J. Alloys Compd.*, 691 (2017) 841.
47. K. Jain and K. Jain, *IJCRT*, 9 (2021) 2320.
48. Electrolytic solution test method-covering power. 1996, Mechanical industry standard. JB/T 7704.2-1995. (in Chinese).